

Article

Pairing Hamiltonians of Nearest-Neighbor Interacting Superconducting Qubits on an IBM Quantum Computer

Shirshendu Chatterjee ¹, Bikash K. Behera ² and Felix J. Seo ^{3,*}

¹ Department of Electrical and Computer Engineering, University of California Santa Barbara, Santa Barbara, CA 93106, USA; shirshendu@ucsb.edu

² Bikash's Quantum (OPC) Pvt. Ltd., Balindi, Mohanpur 741246, India; bikas.riki@gmail.com

³ Department of Physics, Hampton University, Hampton, VA 23668, USA

* Correspondence: jaetae.seo@hamptonu.edu

Abstract: A quantum simulation experiment pairing Hamiltonians of nearest-neighbor interacting superconducting qubits was performed with a complete set of algorithms on an IBM Quantum Computer-IBMQ Lima. The experiment revealed that the fidelity is a function of iteration using Suzuki–Trotter decomposition for four different types of nearest-neighbor Heisenberg, XY, transverse, and longitudinal Ising superconducting qubit couplings of Hamiltonians. The experiment displayed the models of how the experimental density matrices shift from the theoretical density matrices and how their behavior changes with different numbers of iterations. It also demonstrated the reconstruction of quantum states and how the states change as a function of iteration with the IBM Quantum Computer-IBMQ Lima. The time evolutions of the states for different models were also shown to predict the dominance of each state.

Keywords: quantum simulation experiment; coupling Hamiltonians of superconducting qubits; fidelity vs. iteration



Citation: Chatterjee, S.; Behera, B.K.; Seo, F.J. Pairing Hamiltonians of Nearest-Neighbor Interacting Superconducting Qubits on an IBM Quantum Computer. *Appl. Sci.* **2023**, *13*, 12075. <https://doi.org/10.3390/app132112075>

Academic Editor: Nikos Konofaos

Received: 21 August 2023

Revised: 6 September 2023

Accepted: 25 October 2023

Published: 6 November 2023



Copyright: © 2023 by the authors. Licensee MDPI, Basel, Switzerland. This article is an open access article distributed under the terms and conditions of the Creative Commons Attribution (CC BY) license (<https://creativecommons.org/licenses/by/4.0/>).

1. Introduction

A simulation of many-body quantum mechanical dynamics is not a simple computational problem due to the exponential growth of complexity [1]. A quantum simulation was proposed to solve such an exponential explosion problem using a controllable quantum system in the early 1980s [2]. It was shown in 1996 [3] that a quantum computer only containing a few particle interactions can be used to efficiently simulate the many-body quantum Hamiltonians [4]. Quantum computation has recently simulated the various dynamics in condensed-matter physics, high-energy physics [5], quantum chemistry and physics [6], high quantum information processing [7], and quantum gravity [8] using a quantum computer with superconducting qubits. In addition, several qubit systems, including neutral atoms [9], ions [10], polar molecules [11], electrons or nuclear spins in semiconductors quantum dots [12], and photons [13], have been proposed for quantum simulating systems. Among the qubit systems, trapped ion qubits [14] and photon qubits [13] have already been experimentally demonstrated to some extent.

Since Benioff proposed a microscopic quantum mechanical model of computers with Turning machines in 1979, and Feynman conjectured that quantum computers can be programmed to simulate any local quantum system [15], the development of quantum computers and quantum systems has continued over the past three decades [16,17]. Quantum computers have a high computational power with a small number of qubits.

Quantum simulations have recently attracted great interest because of their high computational power, less energy consumption, and exponential speed compared to classical computers for the quantum many-body systems in physics [17,18], chemistry [19], and even biology [20]. Many research groups are now actively focusing on the experimental

realization of quantum simulators with tens of qubits, which would be the first practical applications in which quantum computers could outperform their classical counterparts [21].

In the context of type-1 superconductors, pairing Hamiltonians like the BCS Hamiltonian [22] introduces complex long-range many-body interactions that are typically beyond the capabilities of classical computers to solve. Nonetheless, conducting extensive numerical simulations involving these pairing Hamiltonians holds significant value, both in advancing superconducting quantum computing technology and in conducting scientific inquiries into quantum systems within mesoscopic condensed matter, ultra-small metallic grains, and heavy nuclei [23]. An effort has been made to address this challenge through the proposal of a polynomial time quantum algorithm based on nuclear magnetic resonance (NMR) quantum computing [24]. However, it is important to recognize that liquid NMR faces several limitations that impede the scalability of NMR-based quantum computers. Therefore, achieving widespread implementation of the NMR-based quantum algorithm appears unlikely given the current state of technology [25].

Superconducting quantum circuits [26] have experienced rapid advancements over the past few decades, positioning them as highly promising candidates for practical quantum information processing. Their versatility in design and fabrication, cost-effectiveness, and well-established technology make them suitable for scaling up quantum computing. Additionally, substantial progress has been made in the development of other solid-state qubit devices, such as quantum dots in semiconductors [27] and defect systems. In the past few decades, awareness has grown in the scientific world that quantum computation may be a more natural and desirable method of computation than the classical one. The visible difficulty of solving the problem of quantum many-body physics of fermions (and bosons) on a classical computer demands an exponentially large basis set [28]. Lloyd proposed the first technologically feasible design for a quantum computer [15]. The advancement of quantum computing technology has continued and many quantum algorithms are now also available for the practical applications in simulating, computing, factoring, and featuring. Recently, the IBM Q has provided a platform to simulate many quantum problems using the quantum circuits [29,30] with operational gates and algorithms [31,32]. Utilizing the IBM Q Experience platform, a large number of experiments have been performed for quantum information [33–38], quantum simulation [39–42], quantum key distribution [43], quantum teleportation [44], quantum cryptography [45,46], quantum currency [47], quantum devices [48–51], etc.

In this article, four different pairing Hamiltonians of nearest-neighbor interacting superconducting qubits were simulated with a set of complete algorithms which are suitable for a wide range of models, especially superconducting and semiconducting qubit systems. The quantum state tomography was computed and the fidelity as a function of iterations using the Suzuki–Trotter decomposition was calculated for a 2-qubit system. The time evolution of the system by tuning interaction parameters was studied.

2. Model

2.1. Pairing Hamiltonians in Superconductivity

The BCS pairing Hamiltonian has been widely used in different fields of physics—condensed matter physics, nuclear physics, etc. The Hamiltonian is typically expressed in terms of bosonic or fermionic creation (annihilation) operators, $c_{\pm m}^{\dagger}$ and $c_{\pm l}$, and $n_{\pm l}^F = c_{\pm m}^{\dagger} c_{\pm m}$ are fermionic number operators [52]

$$H_{BCS} = \sum_{m=1}^N \frac{\epsilon_m}{2} (n_m^F + n_{-m}^F) + \sum_{l=1}^N \sum_{m=1}^N V_{ml} c_m^{\dagger} c_{-m}^{\dagger} c_{-l} c_l \quad (1)$$

where the matrix elements are real and can be estimated or calculated, e.g., for superconductors, in terms of Coulomb force and the electron phonon interaction. Pairs of fermions are labeled by the quantum numbers m and $-m$, according to the Cooper pair situation where paired electrons have equal energies but opposite momenta and spins: $m = (p, \uparrow)$ and $-m = (-p, \downarrow)$. This is shown in Figure 1. These are time-reversed and degenerate partners

whose energies are considered to be phenomenological parameters. In order to realize the quantum simulation, the BCS Hamiltonian is transformed into a Hamiltonian with Pauli operators which can be mapped on a system of qubits with the algebraic morphism between spins and fermions.

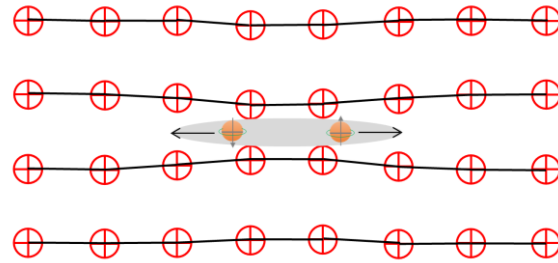


Figure 1. Pictorial representation of the BCS pairing theory.

Then, the fermionic pair operators can be mapped onto a system of qubits which can be represented by the Pauli operators of σ_m^x , σ_m^y , and σ_m^z through the transformation $\{\sigma_m^x, \sigma_m^y, \sigma_m^z\} = \{c_m^\dagger c_{-m}^\dagger + c_{-m} c_m, ic_{-m} c_m + ic_m^\dagger c_{-m}^\dagger, n_m^F + n_{-m}^F - 1\}$.

The transformed Hamiltonian from Equation (1) can be re-written in the qubit form as [52]:

$$H_{BCS} = \sum_{m=1}^N \frac{\epsilon_m}{2} \sigma_m^z + \sum_{m<l} \frac{V_m}{2} (\sigma_m^x \sigma_l^x + \sigma_m^y \sigma_l^y) \tag{2}$$

where $\epsilon_m = \epsilon_m + V_{mm}$.

2.2. Nearest-Neighbor Coupling Interactions in Superconductivity

The coupling of qubits can be achieved through various types of interactions. For superconducting qubits, coupling can be achieved through interactions such as inductance, capacitance, or Josephson junctions. The interaction models can be classified into four categories: XY, Heisenberg, transverse Ising, and longitudinal Ising. These four types of Hamiltonians can be written together as:

$$H = H_0 + H_I \tag{3}$$

H_0 is the single qubit Hamiltonian,

$$H_0 = \sum_{l=1}^N \frac{1}{2} \omega_l \sigma_l^z \tag{4}$$

and H_I denotes the interaction Hamiltonian,

$$H_I = \sum_{l=1}^{N-1} (J_l^x \sigma_l^x \sigma_{l+1}^x + J_l^y \sigma_l^y \sigma_{l+1}^y + J_l^z \sigma_l^z \sigma_{l+1}^z) \tag{5}$$

Here, $\sigma_l^x, \sigma_l^y, \sigma_l^z$ are the Pauli matrices in the basis of σ_l^z and l denotes the l^{th} qubit. The coupling strength between the l^{th} and the $l + 1^{th}$ qubits is denoted by $J_{l,l+1}$ ($l = 1, \dots, N - 1$). The parameters of the previous two equations are chosen to obtain the Hamiltonian of four different models and J_l is fixed accordingly. The different types of interaction hamiltonians are shown in Table 1. It can be seen that the pairing of models in Equation (2) does not follow the form of the Hamiltonians in Equation (3). Thus, it is imperative to design algorithms to simulate these pairing Hamiltonians using the four types of interaction Hamiltonians. For the operators $\sigma_m^x, \sigma_m^y, \sigma_m^z$, care should be taken when simulating the Suzuki–Trotter decomposition, as the operators may not commute. It should be noted that the tunability of parameters ω_l ($l = 1, \dots, N$) and J_l^i ($i = x, y, z, l = 1, \dots, N - 1$) affect the efficiency of the algorithms.

Table 1. Interaction Hamiltonians [52].

Interaction Model	Interaction Hamiltonian
Heisenberg Model	$H_H = H_0 + \sum_{i=x,y,z} \sum_{l=1}^{N-1} J_l^i \sigma_l^i \sigma_{l+1}^i$
XY Model	$H_{XY} = H_0 + \sum_{i=x,y} \sum_{l=1}^{N-1} J_l^i \sigma_l^i \sigma_{l+1}^i$
Transverse Ising Model	$H_{TIsing} = H_0 + \sum_{l=1}^{N-1} J_l \sigma_l^x \sigma_{l+1}^x$
Longitudinal Ising Model	$H_{LIsing} = H_0 + \sum_{l=1}^{N-1} J_l \sigma_l^z \sigma_{l+1}^z$

3. Methods of Simulation for Hamiltonian Operators

The method of simulating the Hamiltonians for each model is shown in Figure 2, where the initial state of the qubits is prepared, the final state is prepared after the unitary operator works on it, and finally the measurement and mapping of the classical register are performed. The final circuit representation of those models is shown in Figure 3. Consecutively these circuits were simulated in the IBM Quantum Computer with the density matrices shown in Figures 4–7 along with time evolution of the quantum states as shown in Figure 8.

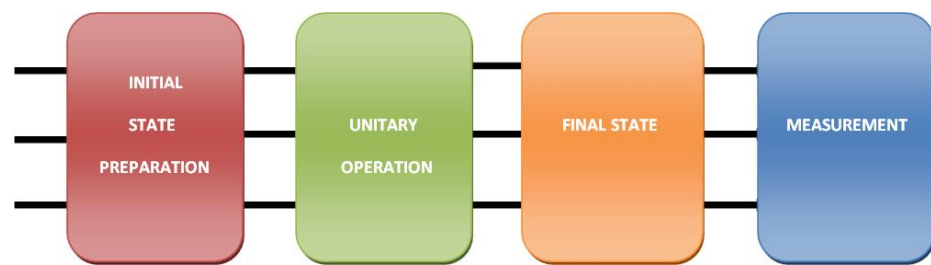


Figure 2. Schematic diagram of the method of simulation of the 2-qubit pairing Hamiltonian.

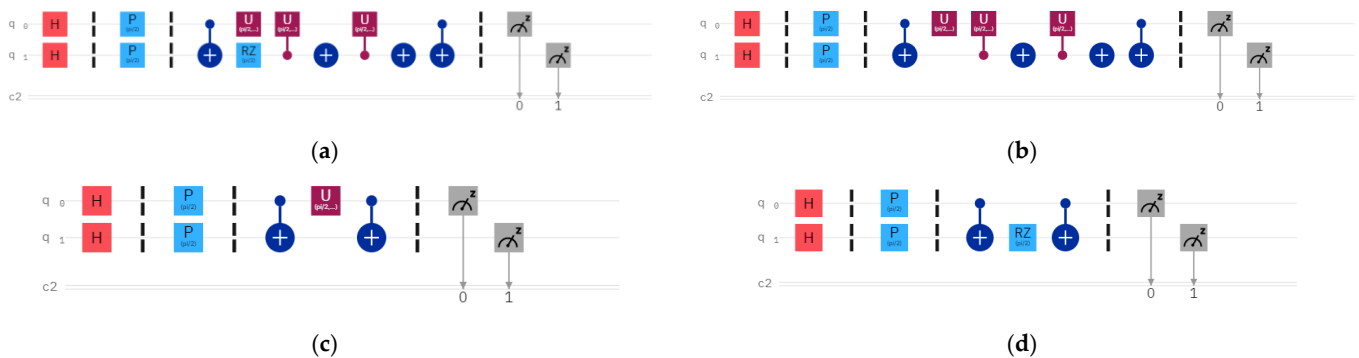


Figure 3. Quantum circuits for the nearest-neighbor interacting (a) Heisenberg, (b) XY, (c) transverse Ising, and (d) longitudinal Ising Hamiltonian models.

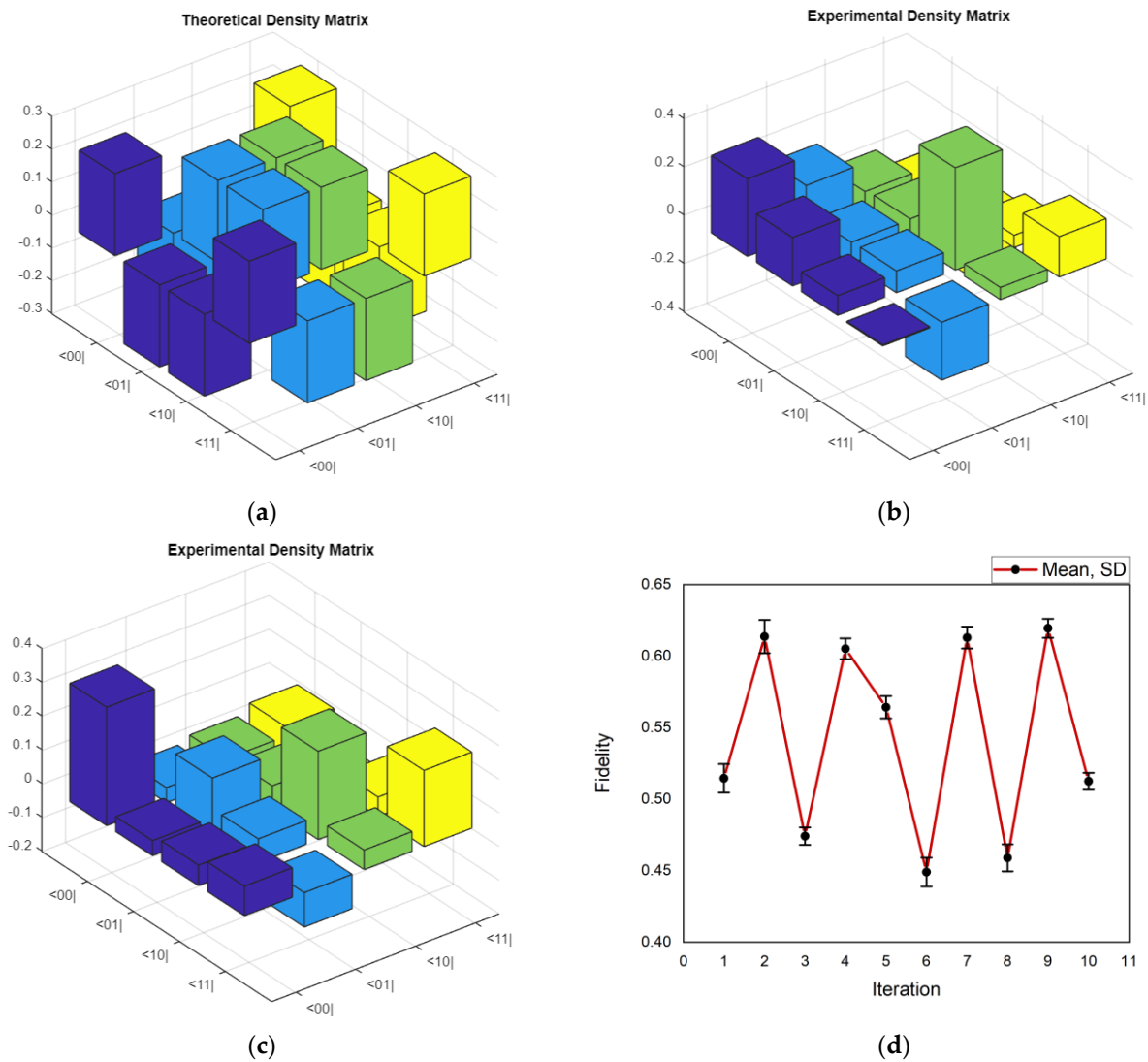


Figure 4. (a) Theoretical density matrix for the Heisenberg model, (b) experimental density matrix for 2 iterations, (c) experimental density matrix for 10 iterations, and (d) fidelity as a function of iteration.

Given the initial state at time $t = 0$, it can be solved to obtain the state at any later instant [53]. If \hat{H} is independent of time, then

$$|\psi(x, t)\rangle = e^{-i\hat{H}t}|\psi(0)\rangle \tag{6}$$

where $U(t) = e^{-i\hat{H}t}$ is the time evolution operator. $U(t)$ is a unitary operator, i.e., $U^\dagger U = I$. For our case, the simulation of four different Hamiltonian was performed to find the corresponding unitary operations to build the quantum circuit.

In general, to find the matrices for the time evolution operator, what the terms $\hat{\sigma}^x$, $\hat{\sigma}^y$, $\hat{\sigma}^z$, $\hat{\sigma}^x \hat{\sigma}^x$, $\hat{\sigma}^y \hat{\sigma}^y$, and $\hat{\sigma}^z \hat{\sigma}^z$ look like needs to be determined. Then, the terms can be separated for x, y, z as $\hat{\sigma}^x \hat{\sigma}^x$, $\hat{\sigma}^y \hat{\sigma}^y$, and $\hat{\sigma}^z \hat{\sigma}^z$ to commute with each other. The Hamiltonian of our choice is

$$H = \sum_{l=1}^N \frac{1}{2} \omega_l \hat{\sigma}_l^z + \sum_{l=1}^{N-1} \left(J_l^x \hat{\sigma}_l^x \hat{\sigma}_{l+1}^x + J_l^y \hat{\sigma}_l^y \hat{\sigma}_{l+1}^y + J_l^z \hat{\sigma}_l^z \hat{\sigma}_{l+1}^z \right) \tag{7}$$

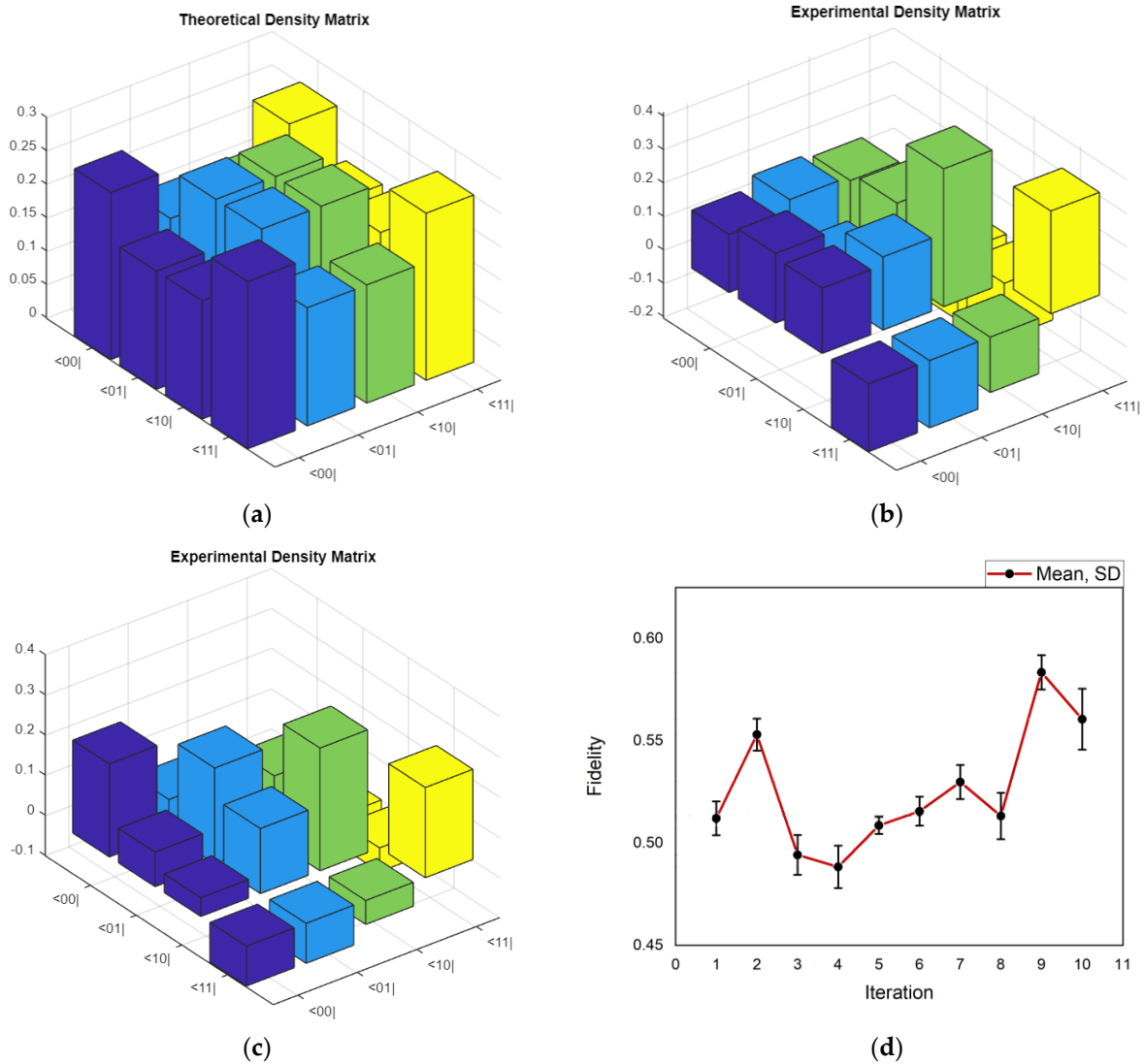


Figure 5. (a) Theoretical density matrix for the XY model, (b) experimental density matrix for 2 iterations, (c) experimental density matrix for 10 iterations, and (d) fidelity as a function of iteration.

The corresponding time evolution operator is given by

$$U(t) = e^{-i(\sum_{i=1}^N \frac{1}{2}\omega_i\sigma_i^z)t} e^{-i\sum_{i=1}^{N-1} (J_i^x\sigma_i^x\sigma_{i+1}^x + J_i^y\sigma_i^y\sigma_{i+1}^y + J_i^z\sigma_i^z\sigma_{i+1}^z)t} \quad (8)$$

Here, $\hat{\sigma}^x = \begin{bmatrix} 0 & 1 \\ 1 & 0 \end{bmatrix}$, $\hat{\sigma}^y = \begin{bmatrix} 0 & -i \\ i & 0 \end{bmatrix}$, and $\hat{\sigma}^z = \begin{bmatrix} 0 & -i \\ i & 0 \end{bmatrix}$.

The first part of the operator can be written as per the value of Pauli matrix $\hat{\sigma}^z$ as shown. The term $e^{-iJ_i\hat{\sigma}^x\hat{\sigma}^x t}$ in the second part of the operator can be written as

$$= \begin{bmatrix} I \cos(J_1 t) - \hat{\sigma}^x \otimes \hat{\sigma}^x i \sin(J_1 t) & & & \\ \cos(J_1 t) & 0 & 0 & -i \sin(J_1 t) \\ 0 & \cos(J_1 t) & -i \sin(J_1 t) & 0 \\ 0 & -i \sin(J_1 t) & \cos(J_1 t) & 0 \\ -i \sin(J_1 t) & 0 & 0 & \cos(J_1 t) \end{bmatrix} \quad (9)$$

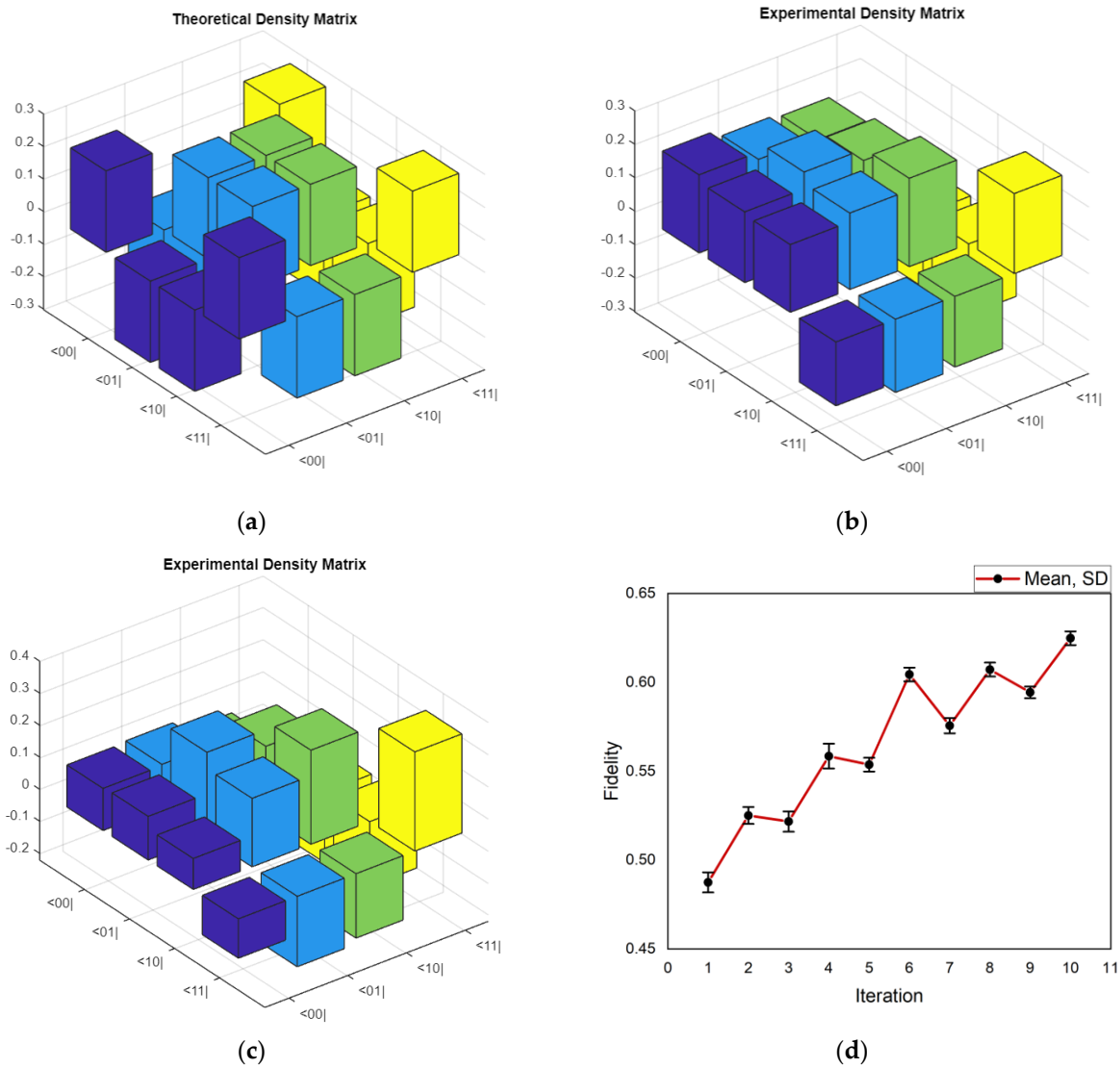


Figure 6. (a) Theoretical density matrix for the transverse Ising model, (b) experimental density matrix for 2 iterations, (c) experimental density matrix for 10 iterations, and (d) fidelity as a function of iteration.

The term $e^{-iJ_I \hat{\sigma}^y \hat{\sigma}^y t}$ in the second part of the operator can be written as

$$\begin{aligned}
 & I \cos J_I t - \hat{\sigma}^y \otimes \hat{\sigma}^y i \sin J_I t \\
 = & \begin{bmatrix} \cos(J_I t) & 0 & 0 & i \sin(J_I t) \\ 0 & \cos(J_I t) & -i \sin(J_I t) & 0 \\ 0 & -i \sin(J_I t) & \cos(J_I t) & 0 \\ i \sin(J_I t) & 0 & 0 & \cos(J_I t) \end{bmatrix} \quad (10)
 \end{aligned}$$

The term $e^{-iJ_I \hat{\sigma}^y \hat{\sigma}^y t}$ in the second part of the operator can be written as

$$\begin{aligned}
 & I \cos J_I t - \hat{\sigma}^y \otimes \hat{\sigma}^y i \sin J_I t \\
 = & \begin{bmatrix} e^{-J_I t} & 0 & 0 & 0 \\ 0 & e^{J_I t} & 0 & 0 \\ 0 & 0 & e^{J_I t} & 0 \\ 0 & 0 & 0 & e^{-J_I t} \end{bmatrix} \quad (11)
 \end{aligned}$$

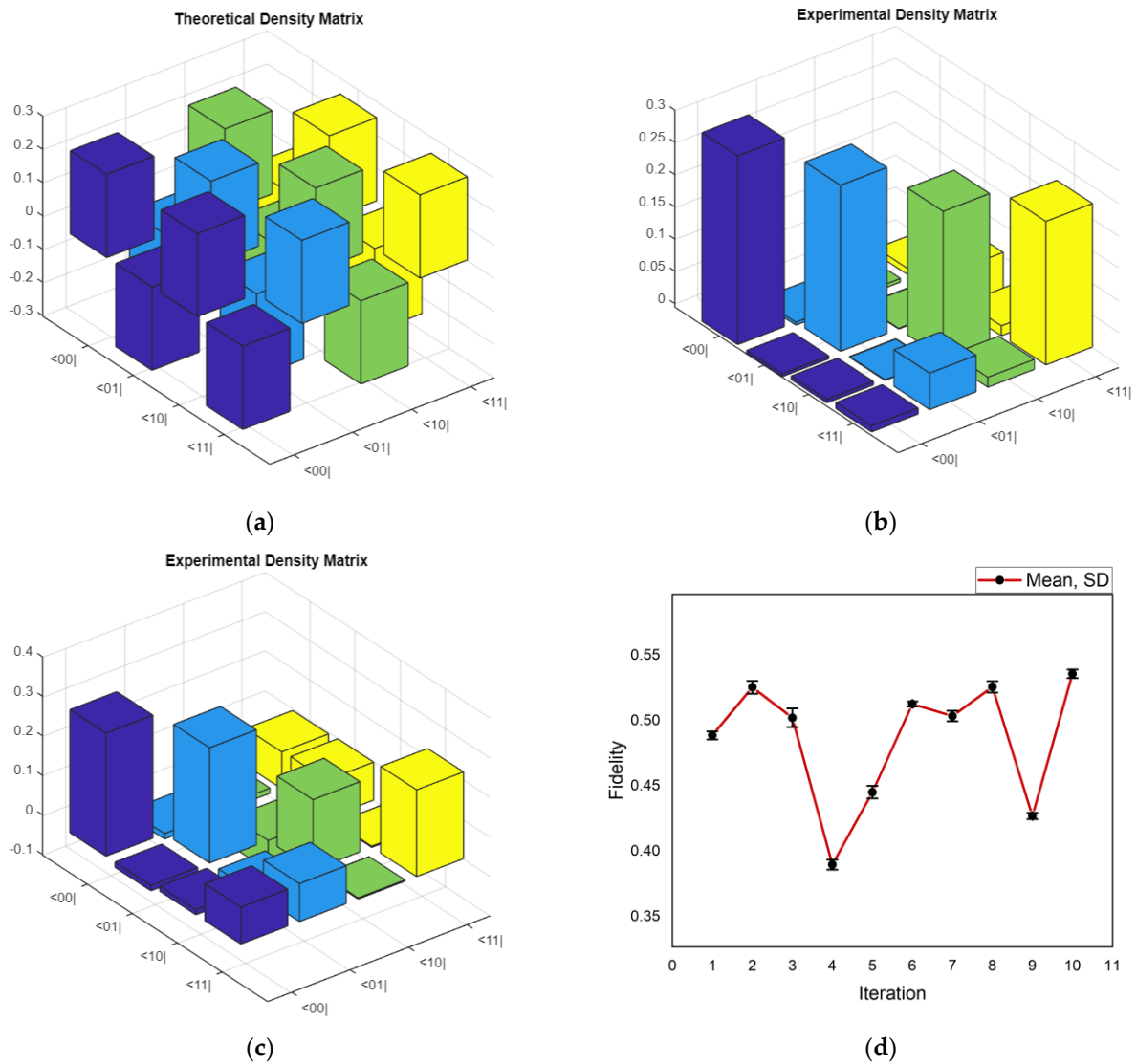


Figure 7. (a) Theoretical density matrix for the longitudinal Ising model, (b) experimental density matrix for 2 iterations, (c) experimental density matrix for 10 iterations, and (d) fidelity as a function of iteration.

Now, referring to the four Hamiltonians, the time evaluation operator can be written and then proceed to implementation. Each of the four types of Hamiltonians is a special case of Equation (7) with its parameters properly chosen. The Hamiltonian can thus be reduced to the (i) longitudinal Ising Hamiltonian for parameters $J_i^x = J_i^y = 0$ and $J_i^z = J_i$; (ii) transverse Ising Hamiltonian for parameters $J_i^y = J_i^z = 0$ and $J_i^x = J_i$; (iii) XY Hamiltonian for parameters $J_i^z = 0$ and $J_i^x = J_i^y = J_i$; and (iv) Heisenberg Hamiltonian for parameters $J_i^x = J_i^y = J_i^z = J_i$.

The following step is to implement the unitary operator in a quantum circuit as obtained from the previous calculations. So, the whole calculation can be elaborated as follows.

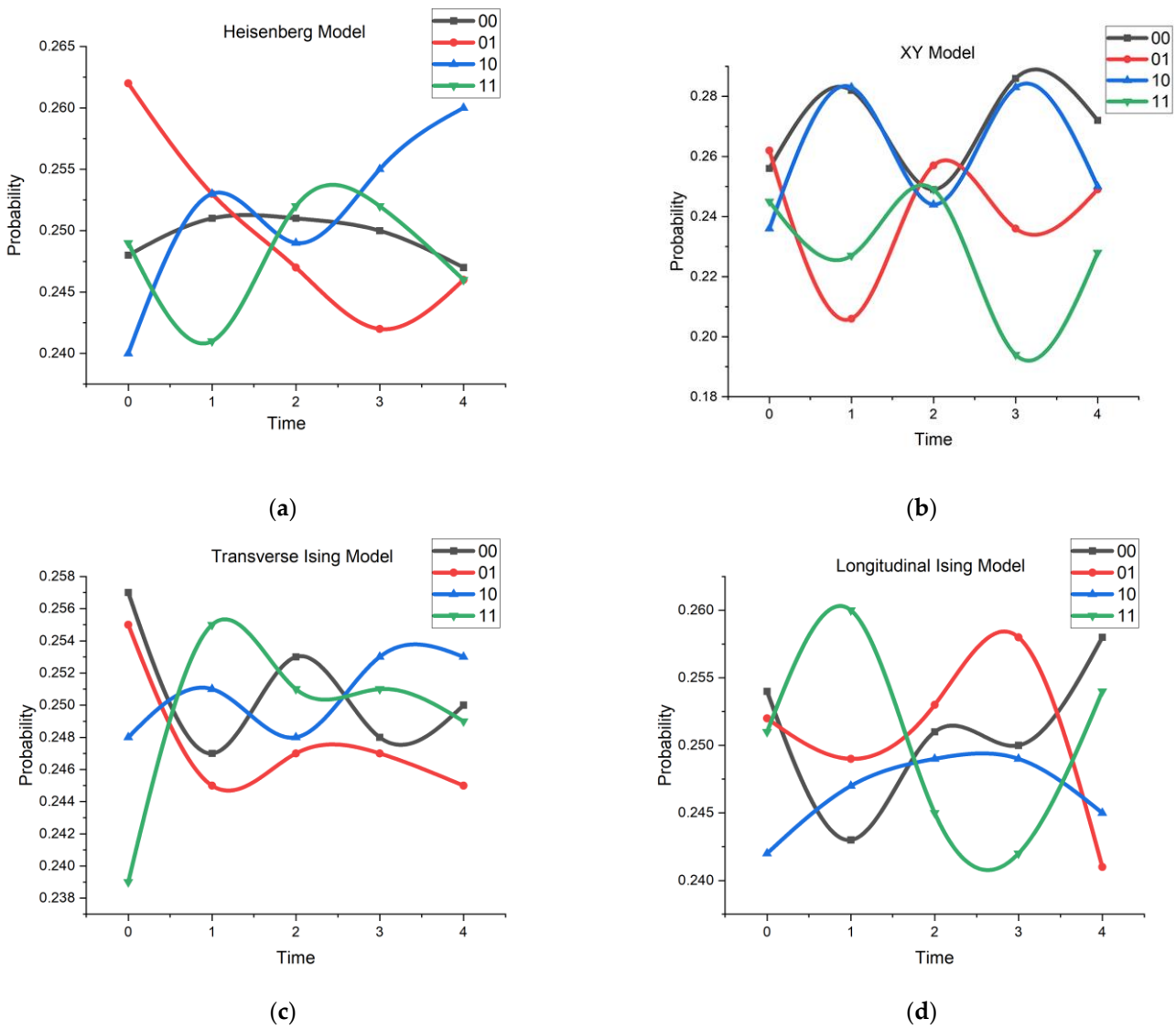


Figure 8. (a) Time evolution of the different models at $\frac{\theta}{2}$ for (a) Heisenberg, (b) XY, (c) transverse Ising, and (d) longitudinal Ising models.

In General

The Hamiltonian is given by

$$H = \sum_{l=1}^N \frac{1}{2} \omega_l \sigma_l^z + \sum_{l=1}^{N-1} \left(J_l^x \sigma_l^x \sigma_{l+1}^x + J_l^y \sigma_l^y \sigma_{l+1}^y + J_l^z \sigma_l^z \sigma_{l+1}^z \right) \quad (12)$$

which is simplified for a 2-qubit system:

$$H = \frac{1}{2} \omega_1 \sigma_1^z + \frac{1}{2} \omega_2 \sigma_2^z + \left(J_1^x \sigma_1^x \sigma_2^x + J_1^y \sigma_1^y \sigma_2^y + J_1^z \sigma_1^z \sigma_2^z \right) \quad (13)$$

For the XX operation:

The term $\hat{\sigma}^x \hat{\sigma}^x$ of the Hamiltonian is to be decomposed to form the circuit.

Let us consider the $U3$ gate:

$$U3(\theta, \phi, \lambda) = \begin{bmatrix} \cos \theta/2 & e^{-i\lambda} \sin \theta/2 \\ e^{i\phi} \sin \theta/2 & e^{i(\phi+\lambda)} \cos \theta/2 \end{bmatrix} \quad (14)$$

$$U3\left(\theta, \phi = -\frac{\pi}{2}, \lambda = \frac{\pi}{2}\right) = \begin{bmatrix} \cos \theta/2 & -i \sin \theta/2 \\ -i \sin \theta/2 & \cos \theta/2 \end{bmatrix}$$

This gate satisfies the conditions for the unitary operator. Thus, it is obtained as $e^{-iJ_1\hat{\sigma}_1^x\hat{\sigma}_2^x t} = (\text{CNOT})_{12}U_{31}(\text{CNOT})_{12}$. This is shown in Figure 9a.

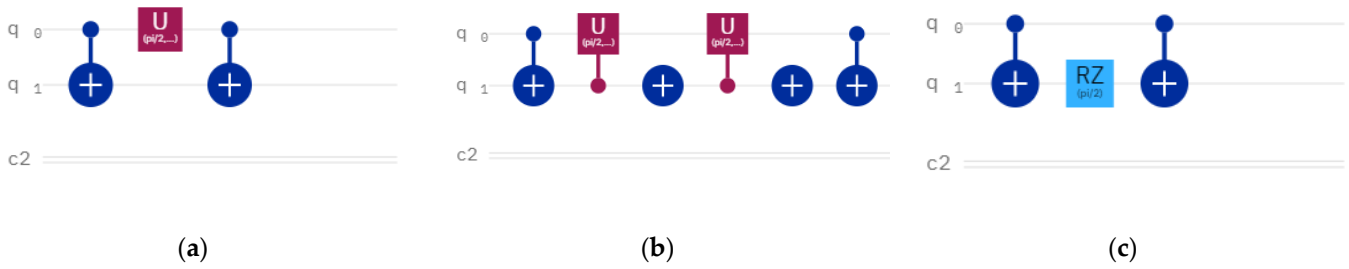


Figure 9. (a) Circuit implementation for the different interactions of the $\hat{\sigma}_1^x\hat{\sigma}_2^x$ term where the circuit consists of two CNOT gates and one U_3 gate; (b) $\hat{\sigma}_1^y\hat{\sigma}_2^y$ term where the circuit consists of two CNOT gates and one U_3 gate, one U_3^\dagger gate and two NOT gates; and (c) $\hat{\sigma}_1^z\hat{\sigma}_2^z$ term where the circuit consists of two CNOT gates and one Rz gate.

For the YY operation:

Similarly, for the $\hat{\sigma}_1^y\hat{\sigma}_2^y$ term, a U_3 gate is to be found. Among the four types of U_3 gates, only the two shown below can be applied.

$$U_3 = \begin{bmatrix} \cos \frac{\theta}{2} & i \sin \frac{\theta}{2} \\ i \sin \frac{\theta}{2} & \cos \frac{\theta}{2} \end{bmatrix}, U_3^\dagger = \begin{bmatrix} \cos \frac{\theta}{2} & -i \sin \frac{\theta}{2} \\ -i \sin \frac{\theta}{2} & \cos \frac{\theta}{2} \end{bmatrix} \tag{15}$$

Thus, $e^{-iJ_1\hat{\sigma}_1^y\hat{\sigma}_2^y t} = (\text{CNOT})_{12} \cdot U_{321} \cdot U_{321}^\dagger \cdot (\text{CNOT})_{12}$.

This is shown in Figure 9b.

For the ZZ operation:

Similarly, for the $\hat{\sigma}_1^z\hat{\sigma}_2^z$ term, let us consider the Rz gate

$$R_z = \begin{bmatrix} e^{-i\frac{\theta}{2}} & 0 \\ 0 & e^{i\frac{\theta}{2}} \end{bmatrix} \tag{16}$$

This equation satisfies the above conditions. While performing the calculations, it can be observed that $e^{-iJ_1\hat{\sigma}_1^z\hat{\sigma}_2^z t} = (\text{CNOT})_{12}R_{z2}(\text{CNOT})_{12}$. This is shown in Figure 9c.

Thus, the circuit is completed for the Hamiltonian in general. Now, this calculation is extended for the Heisenberg model, XY model, transverse Ising model, and longitudinal Ising model. The circuits for the four different models are shown in Figure 3.

4. Results

4.1. Initial State Preparation and Unitary Operation

The initial state is prepared by superposing the states of two qubits required to define the pairing Hamiltonian. This is performed by placing a Hadamard gate on each qubit which provides the contributions of all the qubits to the measurement. The unitary operators obtained in the previous section corresponding to the XX, YY, and ZZ types of interaction are then converted into quantum gates [32] and applied to form a circuit.

- For the XX type of interaction: Comparing with the standard U_3 gate (Equation (15)), the parameters for the gate are found to be $\theta = 2J_1t$, $\phi = -\pi/2$, and $\lambda = \pi/2$;
- For the YY type of interaction: The parameters obtained for the U_3 gate are $\theta = 2J_1t$, $\phi = -\pi/2$, and $\lambda = \pi/2$. The parameters obtained for the U_3^\dagger gate are $\theta = 2J_1t$, $\phi = \pi/2$, and $\lambda = -\pi/2$;

- For the ZZ type of interaction: Comparing with the standard $U1$ gate,

$$U1 = \begin{bmatrix} 1 & 0 \\ 0 & e^{i\lambda} \end{bmatrix} \quad (17)$$

$$\lambda = 2J_1 t,$$

4.2. Quantum State Tomography for Suzuki–Trotter Decomposition of Quantum Circuits

In this section, Suzuki–Trotter decomposition is used to count the fidelity as a function of iterations of the quantum circuit. The circuit was iterated for $n = 1, 2, 3, 4, 5, 6, 7, 8, 9,$ and 10 . Quantum state tomography [54] was used to obtain the theoretical and experimental density matrices, thus calculating the fidelity [55–57] of the circuit as shown in Equation (18).

$$F(\rho, \sigma) = \text{tr} \sqrt{\sqrt{\rho} \sigma \sqrt{\rho}} \quad (18)$$

The general form of quantum state tomography is given by

$$\rho = \frac{1}{2^N} \sum_{l=i_1, i_2, \dots, i_N=0}^1 T_{i_1, i_2, \dots, i_N} \sigma_{i_1} \otimes \sigma_{i_2} \otimes \dots \otimes \sigma_{i_N} \quad (19)$$

In particular, quantum state tomography reconstructs the density matrix of a quantum state by preparing the state many times and measuring each in a tomographically complete basis of measurement operators. In this paper, the circuit was measured with measurements of all qubits in each of the X, Y, and Z Pauli bases. For the 2-qubit system, these basis are II, IX, IY, IZ, XI, YI, ZI, XX, XY, XZ, YX, YY, YZ, ZX, ZY, and ZZ. The probabilities of the states were taken by the experiment in the IBM real superconducting chip- IBMq Lima and the density matrix was constructed by using the formula given in Equation (19).

The experimental matrices of the circuits were computed through the density matrix as shown above. The experimental density matrix and the theoretical density matrix were compared and the fidelity of the quantum circuits was thus calculated. The whole circuit was simulated in “IBMQ-Lima”.

It is important to know the parameters of the qubit system that is used in the experimental process. These parameters are shown in Figure 10, which shows a map view of the qubits, T1 (relaxation time) and T2 (dephasing time), and the frequency of each qubit [58,59]. Here, the T1 (or longitudinal) relaxation process involves a loss of energy of the qubit. It is a relaxation from the excited to the ground state (hence, longitudinal) and the corresponding timescale is the T1 time, while the T2 (or transverse) relaxation time or phase coherence time, describes how long the phase information of the superposition state of the qubit can be preserved.

Probabilistic simulations and calculations for the quantum systems are usually carried out using the Monte Carlo method on a classical computer. Such methods were used to overcome the setback from the exponentially growing phase spaces. Meanwhile, a quantum simulator [60] is usually very much under the control of the experimenter, and it is capable of simulating the dynamical behaviors of the physical models. Irrespective of the degree of internal correlations or entanglement between the degrees of freedom of the model, it can perform its job efficiently [61].

In this section, the observations corresponding to the different circuits designed during quantum simulation of the pairing Hamiltonian in superconductivity are explained. Figures 4–7 display the theoretical and experimental density matrices, and the fidelity as a function of iterations for the Heisenberg, XY, transverse Ising, and longitudinal Ising models. The plots of the experimental density matrix of 2 and 10 iterations were selected to show the extremities of the iterations that were conducted. This shows how the density matrices are changing toward the theoretical density matrix as we increase the number of iterations. This increase is similar to the theoretical density matrix, as the iteration increases which is a consequence of the Trotter decomposition.

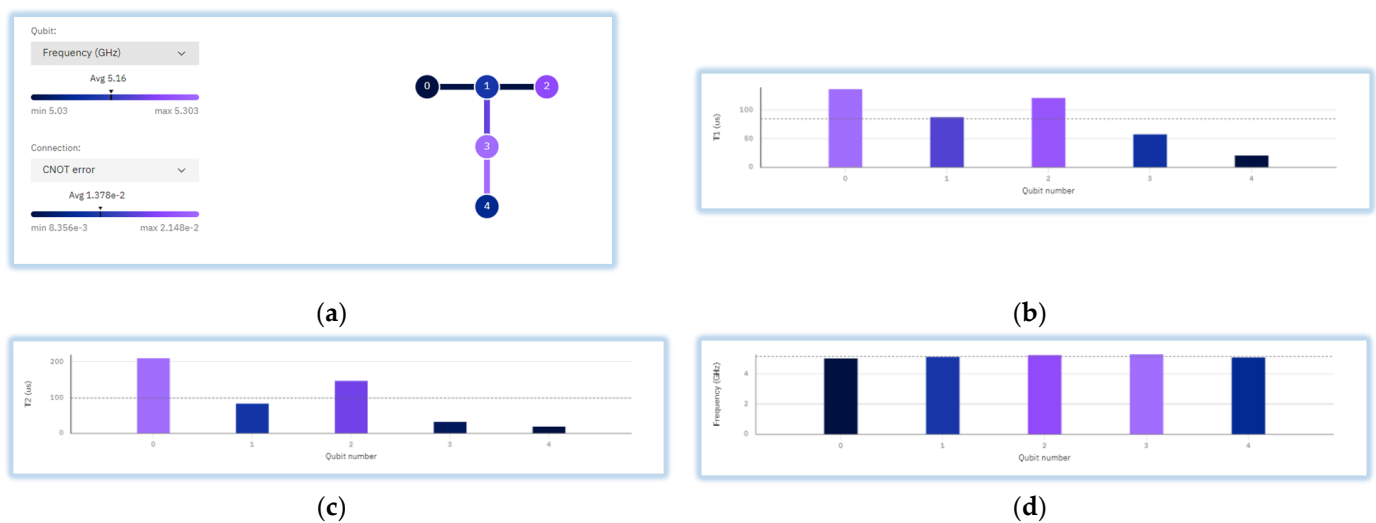


Figure 10. Properties of the quantum processor used: (a) map view of the IBMQ Lima quantum processor, (b) T1 (thermal relaxation time) of the qubits from qubit 0–4, (c) T2 (dephasing time) of the qubits from qubit 0–4, and (d) frequency of operation of the different number of qubits.

It can be seen in Figure 4 that, for the Heisenberg model, the experimental density matrix deviates clearly from the theoretical density matrix. Changes in the experimental density matrix can also be seen as the number of iterations is increased. The fidelity was thus found to be oscillating until 10 iterations. This change corresponds to the increase in probability of a state as the number of iterations increases. This also took a toll on the fidelity of the system as a whole. The error for every iteration was checked and a graph was plotted to check the trend of variation. The variation of fidelity in the system shows the noise in the existing quantum processor. The average fidelity obtained for the system was around 0.55 for the Heisenberg model. In Figure 5, for the XY model, it was seen that the experimental density matrix changed as the number of iterations increased. This is again due to the change in probability of occurrence of each state at a certain iteration. As per the fidelity vs. iteration plot, the fidelity increased from 1 to 2 iterations, then decreased until 4 iterations. The fidelity then increased from 5 iterations until 7 iterations, decreased at 8 iterations, and again increased at 9 iterations and then decreased afterward. The graph shows the trend of these changes. Variations in noise in the system may give such erratic results, although an average value of the fidelity can be obtained to be within 0.5–0.55. For the transverse Ising model (Figure 6), the experimental density matrix figures also changed with increasing number of iterations. The fidelity of the circuit increased from 1 iteration to 10 iterations but showed an erratic pattern. The average value of fidelity for this model was within 0.5–0.6. Finally, for the longitudinal Ising model (Figure 7), the experimental density matrix changed with increasing number of iterations from 2 to 10. The fidelity of the circuit followed the same pattern as the other Hamiltonians, showing an erratic pattern. The average fidelity fell between 0.4–0.55 for this model.

The variation in the fidelity shown for the four models can be attributed to the inclusion of noise from the real chip quantum computer. The noise parameter followed a periodic pattern which affected the fidelity of the circuits, thus showing a near periodic variation in the fidelity. Other than the noise parameter which certainly affected the fidelity, there were a few more findings which we could interpret from that. As per the Trotter decomposition, as we increase the number of iterations, the fidelity of the circuit should increase. But again, in the real experimental circuit inclusion of higher numbers of gates as we increased the number of iterations, it would affect the fidelity so that it decreases. The fluctuations in the fidelity that we see is the effect of both of these parameters. It should also be mentioned that the data points in the graph are low, and thus we can see such fluctuations. But if

we increase the iterations to higher values to fit the graph, we would see that the fidelity would decrease and converge to zero.

In theory, if the number of gates increases in a circuit due to inclusion of more noise, it is expected that the fidelity will decrease. But in the experimental regime, this trend may be affected and can also give a higher fidelity for systems with more gates, as seen in some of the models above.

Figure 8 shows the variation in probability of possible states with respect to different values at $\theta = \frac{\pi}{2}$ and as the time varies for $t = 0, \dots, 4$. For the Heisenberg model, it can be seen that the state $|01\rangle$ is dominant at $t = 0$ s, which decreases to the lowest level at $t = 4$ s. For the XY model, the dominant state is $|01\rangle$ at time $t = 0$ s and state $|00\rangle$ at $t = 4$ s. For the transverse Ising model, the dominant state at $t = 0$ s is $|00\rangle$ while at $t = 4$ s, the dominant state is $|01\rangle$. For the longitudinal Ising model, the dominant state at $t = 0$ s is $|00\rangle$ while at $t = 4$ s, the dominant state is $|00\rangle$. The oscillatory behavior of the plots comes from how the time evolution operator works, i.e., how the unitary operator changes in the states in the Bloch sphere.

5. Conclusions

This article presented algorithms and circuit designs for simulating pairing Hamiltonians based on various nearest-neighbor interactions, such as the Heisenberg Hamiltonian, longitudinal Ising Hamiltonian, XY Hamiltonian, and transverse Ising Hamiltonian, all of which can be executed on solid-state quantum devices. These Hamiltonians were implemented using an IBM superconducting qubit quantum computer. The study involved quantum state tomography for these diverse Hamiltonians, examining fidelity in relation to number of iterations using Suzuki–Trotter decomposition. The experimental density matrix was observed to gradually converge toward the theoretical density matrix as the number of iterations increased. This demonstrates the potential for transforming Hamiltonians from various models into quantum circuits and simulating them on quantum computers to address complex physics problems. Quantum state tomography emerged as a valuable approach for determining the density matrices of such models. By increasing the number of iterations through Trotter decomposition, the experimental outcomes on quantum hardware closely matched the theoretical predictions. The fidelity versus iteration analysis served as a metric to assess how the experimental matrix evolved with increasing number of iterations. This variation in fidelity also highlighted the presence of noise in the quantum system, an inherent characteristic of the “Noisy Intermediate Scale Quantum (NISQ)” era.

Author Contributions: Conceptualization, B.K.B. and F.J.S.; methodology, S.C.; formal analysis, S.C.; resources, S.C., B.K.B. and F.J.S.; data curation, S.C., B.K.B. and F.J.S.; writing—original draft preparation, S.C.; writing—review and editing, B.K.B. and F.J.S.; visualization, S.C.; supervision, B.K.B. and F.J.S.; funding acquisition, F.J.S. All authors have read and agreed to the published version of the manuscript.

Funding: This work at Hampton University was supported by NASA NNX15AQ03A and ARO W911NF-15-1-0535.

Institutional Review Board Statement: Not applicable.

Informed Consent Statement: Not applicable.

Data Availability Statement: The data presented in this study are available in the article.

Acknowledgments: The authors acknowledge the support of IBM Quantum Experience for providing the access to quantum processors. The views expressed are those of the authors and do not reflect the official policy or position of IBM or the IBM Quantum Experience team.

Conflicts of Interest: Author Bikash K. Behera was employed by the company Bikash’s Quantum (OPC) Pvt. Ltd. The remaining authors declare that the research was conducted in the absence of any commercial or financial relationships that could be construed as a potential conflict of interest.

References

1. Smith, A.; Kim, M.S.; Pollmann, F.; Knolle, J. Simulating quantum many-body dynamics on a current digital quantum computer. *npj Quantum Inf.* **2019**, *5*, 106. [[CrossRef](#)]
2. Schirmer, S.G.; Pullen, I.C.; Solomon, A.I. Controllability of Quantum Systems. *IFAC Proc.* **2003**, *36*, 281–286. [[CrossRef](#)]
3. Lloyd, S. Universal quantum simulators. *Science* **1996**, *273*, 1073–1078. [[CrossRef](#)] [[PubMed](#)]
4. Shabani, A.; Mohseni, M.; Lloyd, S.; Kosut, R.L.; Rabitz, H. Rabitz Estimation of many-body quantum Hamiltonians via compressive sensing. *Phys. Rev. A* **2011**, *84*, 012107. [[CrossRef](#)]
5. Nachman, B.; Provasoli, D.; De Jong, W.A.; Bauer, C.W. Quantum algorithm for high energy physics simulations. *Phys. Rev. Lett.* **2021**, *126*, 062001. [[CrossRef](#)] [[PubMed](#)]
6. Lu, D.; Xu, B.; Xu, N.; Li, Z.; Chen, H.; Peng, X.; Xua, R.; Du, J. Quantum chemistry simulation on quantum computers: Theories and experiments. *Phys. Chem. Chem. Phys.* **2012**, *14*, 9411–9420. [[CrossRef](#)] [[PubMed](#)]
7. Langer, C. *High Fidelity Quantum Information Processing with Trapped Ions*; University of Colorado at Boulder: Boulder, CO, USA, 2006.
8. Cohen, L.; Brady, A.J.; Huang, Z.; Liu, H.; Qu, D.; Dowling, J.P.; Han, M. Efficient Simulation of Loop Quantum Gravity: A Scalable Linear-Optical Approach. *Phys. Rev. Lett.* **2021**, *126*, 020501. [[CrossRef](#)]
9. Saffman, M. Quantum computing with neutral atoms. *Natl. Sci. Rev.* **2019**, *6*, 24–25. [[CrossRef](#)]
10. Salari, V.; Naeij, H.; Shafiee, A. Quantum Interference and Selectivity through Biological Ion Channels. *Sci. Rep.* **2017**, *7*, 41625. [[CrossRef](#)]
11. DeMille, D. Quantum Computation with Trapped Polar Molecules. *Phys. Rev. Lett.* **2002**, *88*, 067901. [[CrossRef](#)]
12. Shi, X.-F. Rydberg quantum computation with nuclear spins in two-electron neutral atoms. *Front. Phys.* **2021**, *16*, 1–18. [[CrossRef](#)]
13. Milburn, G. Photons as qubits. *Phys. Scr.* **2009**, *2009*, 014003. [[CrossRef](#)]
14. Blatt, R.; Roos, C.F. Quantum simulations with trapped ions. *Nat. Phys.* **2012**, *8*, 277–284. [[CrossRef](#)]
15. Feynman, R.P. Simulating physics with computers. *Int. J. Theor. Phys.* **1982**, *21*, 467–488. [[CrossRef](#)]
16. Nielsen, M.A.; Chuang, I.L. *Quantum Computation and Quantum Information*; Cambridge University Press: New York, NY, USA, 2011; p. 708.
17. Georgescu, I.M.; Ashhab, S.; Nori, F. Quantum simulation. *Rev. Mod. Phys.* **2014**, *86*, 153. [[CrossRef](#)]
18. Ma, H.; Govoni, M.; Galli, G. Quantum simulations of materials on near-term quantum computers. *npj Comput. Mater.* **2020**, *6*, 85. [[CrossRef](#)]
19. Babbush, R.; Berry, D.W.; McClean, J.R.; Neven, H. Quantum simulation of chemistry with sublinear scaling in basis size. *npj Quantum Inf.* **2019**, *5*, 92. [[CrossRef](#)]
20. Outeiral, M.C.; Shi, S.J.; Morris, G.M.; Benjamin, S.C.; Deane, C.M. The prospects of quantum computing in computational molecular biology. *WIREs Comp. Mol. Sci.* **2020**, *11*, e1481. [[CrossRef](#)]
21. Faroukh, Y.M. Quantum Computers vs Conventional Computers: A Study on the Larger Scale. 2018, p. 24. Available online: https://www.researchgate.net/publication/323993559_Quantum_Computers_Vs_Conventional_Computers_A_Study_on_the_Larger_Scale (accessed on 24 October 2023).
22. Bardeen, J.; Cooper, L.N.; Schrieffer, J.R. Theory of Superconductivity. *Phys. Rev.* **1957**, *108*, 1175. [[CrossRef](#)]
23. Alhassid, K.N.Y. Nesterov Mesoscopic superconductivity in ultrasmall metallic grains. *AIP Conf. Proc.* **2014**, *1619*, 24.
24. Yang, X.; Wang, A.M.; Xu, F.; Du, J. Experimental simulation of a pairing Hamiltonian on an NMR quantum computer. *Chem. Phys. Lett.* **2006**, *422*, 20–24. [[CrossRef](#)]
25. Di Paolo, A.; Baker, T.E.; Foley, A.; Sénéchal, D.; Blais, A. Efficient modeling of superconducting quantum circuits with tensor networks. *NPJ Quantum Inf.* **2021**, *7*, 11. [[CrossRef](#)]
26. Alferov, Z.I. The history and future of semiconductor heterostructures. *Semiconductors* **1998**, *32*, 1–14. [[CrossRef](#)]
27. Loss, D.; Vincenzo, D.D.P. Quantum computation with quantum dots. *Phys. Rev. A* **1998**, *57*, 120. [[CrossRef](#)]
28. Ortiz, G.; Gubernatis, J.E.; Knill, E.; Laflamme, R. Quantum algorithms for fermionic simulations. *Phys. Rev. A* **2001**, *64*, 022319. [[CrossRef](#)]
29. Houck, A.; Tureci, H.; Koch, J. On-chip quantum simulation with superconducting circuits. *Nat. Phys.* **2012**, *8*, 292–299. [[CrossRef](#)]
30. Barends, R.; Kelly, J.; Megrant, A.; Veitia, A.; Sank, D.; Jeffrey, E.; White, T.C.; Mutus, J.; Fowler, A.G.; Campbell, B.; et al. Superconducting quantum circuits at the surface code threshold for fault tolerance. *Nature* **2014**, *508*, 500–503. [[CrossRef](#)]
31. Pathak, A. *Elements of Quantum Computation and Quantum Communication*; Taylor & Francis: Milton Park, UK, 2013.
32. Wikipedia. Quantum Logic Gate. Available online: https://en.wikipedia.org/wiki/Quantum_logic_gate (accessed on 12 February 2019).
33. Devoret, M.H.; Schoelkopf, R.J. Superconducting circuits for quantum information: An outlook. *Science* **2013**, *339*, 1169–1174. [[CrossRef](#)]
34. Clarke, J.; Wilhelm, F.K. Superconducting quantum bits. *Nature* **2008**, *453*, 1031–1042. [[CrossRef](#)] [[PubMed](#)]
35. You, J.Q.; Franco, N. Superconducting Circuits and Quantum Information. *Phys. Today* **2005**, *58*, 42–47. [[CrossRef](#)]
36. Wu, L.A.; Byrd, M.S.; Lidar, D.A. Polynomial-time simulation of pairing models on a quantum computer. *Phys. Rev. Lett.* **2002**, *89*, 057904. [[CrossRef](#)] [[PubMed](#)]
37. Orlando, T.P.; Mooij, J.E.; Tian, L.; van der Wal, C.H.; Levitov, L.S.; Lloyd, S.; Mazo, J.J. Superconducting persistent-current qubit. *Phys. Rev. B* **1999**, *60*, 15398. [[CrossRef](#)]

38. You, J.Q.; Tsai, J.S.; Nori, F. Scalable Quantum Computing with Josephson Charge Qubits. *Phys. Rev. Lett.* **2002**, *89*, 197902. [[CrossRef](#)]
39. Gangopadhyay, S.; Manabputra; Behera, B.K.; Panigrahi, P.K. Generalization and demonstration of an entanglement-based Deutsch-Jozsa-like algorithm using a 5-qubit quantum computer. *Quantum Inf. Process.* **2018**, *17*, 160. [[CrossRef](#)]
40. Mandviwalla, A.; Ohshiro, K.; Ji, B. Implementing Grover's Algorithm on the IBM Quantum Computers. In Proceedings of the 2018 IEEE International Conference on Big Data (Big Data), Seattle, WA, USA, 10–13 December 2018; pp. 2531–2537.
41. Stenger, J.P.T.; Bronn, N.T.; Egger, D.J.; Pekker, D. Simulating the dynamics of braiding of Majorana zero modes using an IBM quantum computer. *Phys. Rev. Res.* **2021**, *3*, 033171. [[CrossRef](#)]
42. Cattaneo, M.M.; Rossi, A.C.; García-Pérez, G.; Zambrini, S.R. Quantum Simulation of Dissipative Collective Effects on Noisy Quantum Computers. *PRX Quantum* **2023**, *4*, 010324. [[CrossRef](#)]
43. Sarkar, K.; Behera, B.K.; Panigrahi, P.K. A Robust Tripartite Quantum Key Distribution Using Mutually Share Bell States and Classical Hash Values Using a Complete Graph Network Architecture. 2019. Available online: https://www.researchgate.net/publication/333148981_A_robust_tripartite_quantum_key_distribution_using_mutually_shared_Bell_states_and_classical_hash_values_using_a_complete-graph_network_architecture (accessed on 24 October 2023).
44. Agarwal, R.; Sethi, C.K.; Gupta, N.K.; Panigrahi, P.K. Comparison of Advantages in Quantum Teleportation Using Cluster State and Coined Quantum Walks. 2020. Available online: https://www.researchgate.net/publication/339528565_Comparison_of_advantages_in_quantum_teleportation_using_cluster_state_and_coined_quantum_walks?channel=doi&linkId=5e578b4092851cefa1c7fd92&showFulltext=true (accessed on 24 October 2023).
45. Warke, A.; Behera, B.K.; Panigrahi, P.K. Experimental Realization of Three Quantum Key Distribution Protocols. *Quantum Inf. Process.* **2020**, *19*, 1–15. [[CrossRef](#)]
46. Saini, R.; Papneja, A.; Behera, B.K.; Panigrahi, P.K. Experimental Realization of Differential Phase Shift Quantum Key Distribution on IBM QX. 2019. Available online: https://www.researchgate.net/publication/337685592_Experimental_Realization_of_Differential_Phase_Shift_Quantum_Key_Distribution_on_IBM_QX?channel=doi&linkId=5de5b14b4585159aa45acc8&showFulltext=true (accessed on 24 October 2023).
47. Behera, B.K.; Banerjee, A.; Panigrahi, P.K. Experimental realization of quantum cheque using a five-qubit quantum computer. *Quantum Inf. Process.* **2017**, *16*, 312. [[CrossRef](#)]
48. Behera, B.K.; Reza, T.; Gupta, A.; Panigrahi, P.K. Designing Quantum Router in IBM Quantum Computer. *Quantum Inf. Process.* **2019**, *18*, 328. [[CrossRef](#)]
49. Behera, B.K.; Seth, S.; Das, A.; Panigrahi, P.K. Demonstration of Entanglement Purification and Swapping Protocol to Design Quantum Repeater in IBM Quantum Computer. *Quantum Inf. Process.* **2019**, *18*, 108. [[CrossRef](#)]
50. McDermott, R.; Simmonds, R.W.; Steffen, M.; Cooper, K.B.; Cicak, K.; Osborn, K.D.; Oh, S.; Pappas, D.P.; Martinis, J.M. Simultaneous state measurement of coupled Josephson phase qubits. *Science* **2005**, *307*, 1299–1302. [[CrossRef](#)]
51. Isaac, D.W.L.; Chuang, L.; Yamaguchi, F.; Yamamoto, Y. Efficient implementation of coupled logic gates for quantum computation. *Phys. Rev. A* **2000**, *61*, 042310.
52. Wang, Z.; Gu, X.; Wu, L.-A.; Liu, Y.-X. Quantum simulation of pairing hamiltonians with nearest-neighbor interacting qubits. *Phys. Rev. A* **2016**, *93*, 062301. [[CrossRef](#)]
53. Griffiths, D.J. *Introduction to Quantum Mechanics*, 2nd ed.; Cambridge University Press: Cambridge, UK, 2017; ISBN 978-1-107-17986-8. OCLC 952389109.
54. Altepeter, J.B.; James, D.F.; Kwiat, P.G. 4 Qubit Quantum State Tomography. In *Quantum State Estimation; Lecture Notes in Physics*; Paris, M., Řeháček, J., Eds.; Springer: Berlin, Heidelberg, 2004; Volume 649.
55. Jozsa, R. Fidelity for Mixed Quantum States. *J. Mod. Opt.* **1994**, *41*, 2315–2324. [[CrossRef](#)]
56. Uhlmann, A. The “transition probability” in the state space of a *-algebra. *Rep. Math. Phys.* **1976**, *9*, 273–279. [[CrossRef](#)]
57. Pedersen, L.H.; Møller, N.M.; Mølmer, K. Fidelity of quantum operations. *Phys. Lett. A* **2007**, *367*, 47–51. [[CrossRef](#)]
58. Carroll, M.; Rosenblatt, S.; Jurcevic, P.; Lauer, I.; Kandala, A. Dynamics of superconducting qubit relaxation times. *NPJ Quantum Inf.* **2022**, *8*, 132. [[CrossRef](#)]
59. Choi, Y.; Joynt, R. Anisotropy with respect to the applied magnetic field of spin qubit decoherence times. *NPJ Quantum Inf.* **2022**, *8*, 70. [[CrossRef](#)]
60. Barreiro, J.T.; Müller, M.; Schindler, P.; Nigg, D.; Monz, T.; Chwalla, M.; Hennrich, M.; Roos, C.F.; Zoller, P.; Blatt, R. An open system quantum simulator with trapped ions. *Nature* **2011**, *470*, 486–491. [[CrossRef](#)]
61. Tacchino, F.; Chiesa, A.; Carretta, S.; Gerace, D. Quantum computers as universal quantum simulators: State of art and perspectives. *Adv. Quantum Technol.* **2020**, *3*, 1900052. [[CrossRef](#)]

Disclaimer/Publisher's Note: The statements, opinions and data contained in all publications are solely those of the individual author(s) and contributor(s) and not of MDPI and/or the editor(s). MDPI and/or the editor(s) disclaim responsibility for any injury to people or property resulting from any ideas, methods, instructions or products referred to in the content.